Available online at www.sciencedirect.com
ScienceDirect
Journal of Power Sources 159 (2006) 1123–1141
JOURNAL OF POWER SOURCES
www.elsevier.com/locate/jpowsour

Modeling non-isothermal two-phase multicomponent flow in the cathode of PEM fuel cells

M. Acosta [a,*], C. Merten [a], G. Eigenberger [a], H. Class [b], R. Helmig [b], B. Thoben [c], H. Müller-Steinhagen [c]

[a] *Institut für Chemische Verfahrenstechnik, Universität Stuttgart, Böblingerstr. 72, D-70199 Stuttgart, Germany*
[b] *Institut für Wasserbau, Universität Stuttgart, Pfaffenwaldring 61, D-70550 Stuttgart, Germany*
[c] *German Aerospace Center, Institut of Technical Thermodynamics, Pfaffenwaldring 38-40, D-70569 Stuttgart, Germany*

Received 6 April 2005; received in revised form 16 December 2005; accepted 21 December 2005
Available online 17 February 2006

Abstract

A two-dimensional, non-isothermal, two-phase, multicomponent model is presented for the cathode of a PEM fuel cell, which can be applied using both conventional and interdigitated gas distributors. Gas and liquid transport are described by an extended Darcy's law using a continuum approach. The most important material properties like wettability, permeability, porosity and tortuosity are determined experimentally. For the determination of the capillary pressure–saturation data, a method based on mercury intrusion porosimetry has been applied. The relative permeability was then derived from this data. It turned out however, that a more detailed description of the partial wetting behaviour of hydrophobic electrodes is of decisive importance. The two-dimensional distribution of the reactants and products is obtained and depends strongly on the flow configuration and the operational conditions. The model results were compared to experimental data and qualitative information on the effects of various operating conditions and on material properties were obtained.

Keywords: PEM; Fuel cell; Multiphase; Flow field; Cathode; Capillary pressure

1. Introduction

Polymer electrolyte membrane (PEM) fuel cells with hydrogen or methanol as fuel are very promising for applications in electrical vehicles and portable power sources and have therefore been intensively investigated during the past decade. Their low operating temperature in the range from ambient temperature up to approximately 100 °C is one of their most important advantages for mobile and portable applications in comparison with other fuel cell types. However, further efforts have to be made in order to improve the performance, reduce the costs, and thus make these systems competitive with conventional energy supplying systems.

The PEM fuel cell consists of a proton conducting polymer membrane situated between two porous catalytic electrodes. Each electrode consists of a porous gas diffusion layer (GDL) or backing, and a reactive layer containing a platinum or platinum alloy catalyst. This membrane-electrode-assembly (MEA) is then placed between two cell plates which provide electrical connection and have flow fields that direct the reactants on the surface of the reactive layer and also permit the removal of the products from the cell.

The chemical reactions in a hydrogen fuel cell are:

- Anode:

$$H_2 \rightarrow 2H^+ + 2e^- \quad (1)$$

- Cathode:

$$\tfrac{1}{2}O_2 + 2H^+ + 2e^- \rightarrow H_2O \quad (2)$$

- Overall:

$$H_2 + \tfrac{1}{2}O_2 \rightarrow H_2O \quad (3)$$

Abbreviations: CCD, charge coupled device; DS, double sided; GDL, gas diffusion layer; HOR, hydrogen oxidation reaction; MEA, membrane-electrode-assembly; ORR, oxygen reduction reaction; PEM, polymer electrolyte membrane; SEM, scanning electron microscopy

* Corresponding author. Tel.: +49 711 6412204; fax: +49 711 6412242.
E-mail address: maria.acosta@iws.uni-stuttgart.de (M. Acosta).

0378-7753/$ – see front matter © 2006 Elsevier B.V. All rights reserved.
doi:10.1016/j.jpowsour.2005.12.068

Nomenclature

A_1	empirical constant in Eq. (27)
A_2	empirical constant in Eq. (28)
B_1	empirical constant in Eq. (27)
B_2	empirical constant in Eq. (28)
c_s	heat capacity of the solid matrix ($J\,kg^{-1}\,K^{-1}$)
C_1	empirical constant in Eq. (27)
C_2	empirical constant in Eq. (28)
D_{eff}	effective diffusion coefficient ($m^2\,s^{-1}$)
D_{ij}	binary diffusion coefficient ($m^2\,s^{-1}$)
D_{pm}	effective diffusion coefficient in porous medium ($m^2\,s^{-1}$)
D_1	empirical constant in Eq. (27)
D_2	empirical constant in Eq. (28)
E_2	empirical constant in Eq. (28)
f_v	catalytic surface increasing factor
F	Faraday's constant, 96484.56 C mol^{-1}
$\mathbf{g}$	gravity vector ($m\,s^{-2}$)
$\Delta G_0^{\neq}$	free activation enthalpy ($J\,mol^{-1}$)
h	enthalpy ($kJ\,kg^{-1}$)
i	current density ($A\,cm^{-2}$)
i_o^{ref}	exchange current density ORR ($A\,cm^{-2}$)
J	diffusive molar flow ($mol\,s^{-1}\,m^{-2}$)
k_r	relative permeability
K	absolute permeability (m^2)
$\dot{N}$	molar flux ($mol\,m^{-2}\,s^{-1}$)
p	pressure (Pa)
p_c	capillary pressure (Pa)
q	source or sink term ($mol\,s^{-1}\,m^{-3}$), heat flux ($J\,s^{-1}\,m^{-2}$)
q^h	energy source or sink term ($J\,s^{-1}\,m^{-3}$)
r	radius (m)
R	universal gas constant (8.314 J mol^{-1} K^{-1})
R_{spec}	specific resistance ($\Omega\,m^2$)
S	phase saturation
S_α	phase saturation
t	transport number, time
T	temperature (K)
u	internal energy ($kJ\,kg^{-1}$)
U_{cell}	cell voltage (V)
U_{oc}	open circuit voltage (V)
U_{rev}	reversible cell voltage (V)
U_{th}	thermoneutral cell voltage (V)
v	Darcy velocity ($m\,s^{-1}$)
x	molar fraction
z	number of transferred electrons

Greek symbols

α	fluid phase, load transfer number in Eq. (12)
δ	thickness (m)
η	overvoltage (V)
η_{equ}	equilibrium overvoltage (V)
η_{trans}	transfer overvoltage (V)
θ	contact angle
λ	thermal conductivity ($W\,K^{-1}\,m^{-1}$)
μ	dynamic viscosity ($kg\,m^{-1}\,s^{-1}$)
ν_i	stoichiometric coefficient
ρ_α	phase density ($kg\,m^3$)
σ	surface tension ($N\,m^{-1}$)
τ	tortuosity
ϕ	porosity

Subscripts and superscripts

a	anode
c	cathode
g	gas phase
H_2O	water component
inlet	cell inlet conditions
K	component
M	membrane
N_2	nitrogen component
O_2	oxygen component
pm	porous medium
r	residual
R	reaction
ref	reference conditions ORR
w	liquid water phase

Potential losses under electrical current occur due to kinetic activation resistances, ohmic losses and mass transfer limitations, as can be recognized from the form of a typical polarization curve [1]. It is an accepted fact that the cathode of the H_2-PEM fuel cell is the performance-limiting component due to the slower kinetics of the oxygen reduction reaction [2] and the mass-transfer limitations for oxygen. They are caused by the stagnant nitrogen (if operated with air) and the counter diffusion of the water vapor formed and are enhanced by the liquid water generated by electrochemical reaction and electro-osmotic drag, which accumulates in the porous catalyst and gas diffusion layers.

The water management in a PEM fuel cell is difficult due to the fact that the membrane has to be humidified to be able to transport the protons from anode to cathode. On the other side, water accumulating in the cathode electrode hinders the oxygen transport to the catalyst layer.

The reactive gases, typically hydrogen and air, normally have to be humidified to avoid dry-out of the membrane. Thus, a gas–liquid, two-phase flow is occurring within the flow field at the cathode, particularly at high current densities when the amount of water from reaction and electro-osmosis are higher. The water phase may flood part of the electrode pores or the channel, hence blocking the oxygen supply to the reactive layer. Liquid water also covers the catalyst sites, thus inhibiting the oxygen reduction reaction (ORR).

The interaction of material properties, cell and electrode design, and the operating conditions affect the water management and thus the performance of the cell. In practice the backing is made of conducting carbon material, which is treated with

Teflon to render it hydrophobic and enhance the liquid water removal. Moreover, new types of flow fields have been developed to improve the gas flow and water transport [3].

Due to the small geometry, the actual reactant and product concentration profiles in the catalyst and gas diffusion layers are very difficult to measure. This has prompted researchers to develop mathematical models to provide qualitative insight into the processes involved in the fuel cell. The modeling has been specially focused on the cathode, due to its importance as performance-limiting component.

Previous studies were mostly based on a simple (gas) phase assumption, with the presence of liquid water being neglected. Many of these models are one-dimensional (dimension normal to the reactive catalyst surface), e.g., [2,4], and also in $1+1$ or two dimensions, e.g., [5–10]. Recently, several studies on two-phase, multidimensional transport in PEMFC have been made [11–20]. Only few investigations [12,17,18] include the energy equation to predict the effect of heat produced by the electrochemical reactions on fuel cell performance. Shimpalee et al. [12], for example, treat the liquid water as a component of the gas mixture and not as a separated phase. Moreover, all these models assume hydrophilic properties of the gas diffusion layers. [20,21] used a Leverett approach and extended it to obtain hydrophobic data for use in their one-dimensional models.

For the typically used hydrophobic carbon gas diffusion materials there is a lack of property data. Most recently, [22] characterized some commercial gas diffusion materials, reporting data like contact angle, permeability, porosity and conductivity. No measured capillary pressures have been published for those materials, mainly due to the difficulty in applying conventional methods, e.g., see [23], to these small dimensioned materials.

In the present study we propose a simple method to determine the capillary pressure–saturation relationship for the usual carbon diffusion layer materials and implement these data in our two-dimensional, non-isothermal, two-phase model. We compare the results with measured polarization curves and use our model to predict the influence of some parameters, like inlet stream humidity and capillarity, on the liquid water distribution and cell performance.

In the following, the governing equations and boundary conditions used in the model are presented in Section 2. The applied numerical discretization technique, given in Section 3, follows. Section 4 shows the experimentally determined modeling parameters followed by the results and discussions in Section 5 and the summary and conclusions of the work, which are given in Section 6.

2. Mathematical model

2.1. Model description and assumptions

Fig. 1 shows a schematic representation of the domain modeled. It is confined to the cathode gas diffusion and catalyst layers in contact with the membrane and with a gas distributor, here shown by two half channels and a shoulder. Depending on the selected boundary conditions at the channel interfaces the operation with conventional straight channel and with interdigitated gas distributors can be modeled.

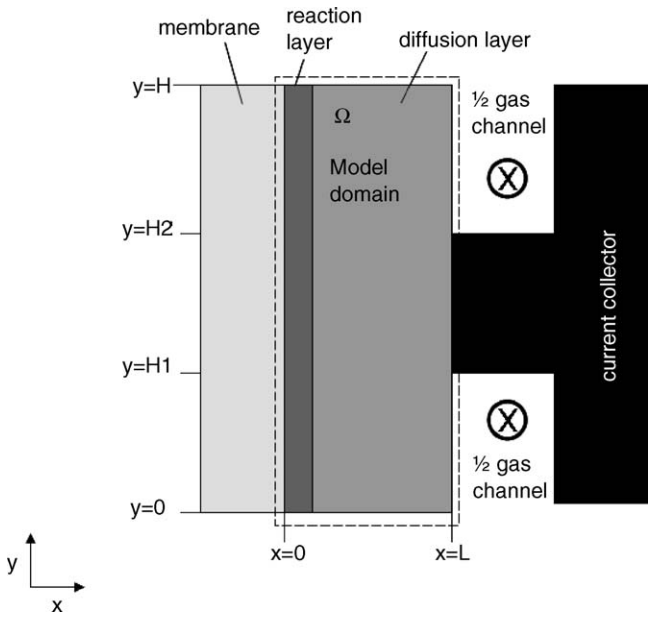

Fig. 1. Two-dimensional model domain.

It has been demonstrated that the main mass transport limitations in PEM fuel cells occur within the electrode (gas diffusion and catalyst) layers [3]. For the case of a conventional flow field, air flows parallel to the gas diffusion layer. The predominant mechanism for oxygen transport within the electrode is diffusion. Liquid water moves due to capillary forces. In the case of interdigitated flow fields the gas is forced to flow through the diffusion layer, hence producing a forced convective mass transfer. Liquid water flows due to both capillary forces and the shear force of the gas stream.

It has been found that the kinetics of the oxygen reduction reaction (ORR) at the cathode is at least five orders of magnitude slower than the hydrogen oxidation reaction (HOR) [24]. The cell overpotential on the anode side is thus neglected, considering the operation with pure hydrogen. The catalyst layer at the cathode is treated as a thin layer where oxygen is depleted and water and heat are produced, defining source and sink terms, respectively. The depletion and production rates depend on the local current density, which is described by the Tafel equation [25]. The local current density is again a function of the local oxygen concentration. No limitations for the proton transport are considered within the catalyst layer. The membrane is assumed to be fully hydrated with liquid water and to have a constant ionic conductivity for the determination of ohmic losses associated with ionic transport.

For the description of the transport of both gas and liquid phases in the porous cathode electrode a continuum approach is adopted, see e.g., [23]. It is also assumed that the system is in local thermodynamic equilibrium. The porous electrode is assumed to be isotropic. This is a simplification for the numerical modeling. The authors are aware that the material can be anisotropic to a certain degree due its structure. Furthermore, an extended Darcy's law is used to describe the movement of both

gas and liquid phases within the porous system. The membrane is considered impermeable for the gases. The ohmic heating in the current collector plate and in the GDL is neglected due to their high conductivity. A part of the heat produced in the electrochemical reaction is transported by conduction through the membrane.

2.2. Governing equations

2.2.1. Multiphase flow in porous media

Using an Eulerian approach, we formulate a balance equation for each of the mass components, assuming that all phases are in local thermodynamic equilibrium. The investigated system is composed of the two phases (α) liquid water and gas, represented by 'w' and 'g', respectively, and the three components (K) H_2O, O_2 and N_2. The mass balance equation per component can be written as

$$\frac{\partial(\sum_\alpha \phi S_\alpha \rho_\alpha x_\alpha^K)}{\partial t} + \sum_\alpha \mathrm{div}\{\rho_\alpha x_\alpha^K v_\alpha + J^K\} - q^K = 0,$$
$$\alpha \in \{\mathrm{w}, \mathrm{g}\}, \quad K \in \{H_2O, O_2, N_2\}, \tag{4}$$

where ϕ represents the porosity, S_α the phase saturation, defined as the volumetric portion of the pore space occupied by the phase α, ρ_α the phase density, x_α^K the molar fraction of component K in phase α, v_α the Darcy velocity, J^K the diffusive flux of component K and q_α represents a source ($q_\alpha > 0$) or sink ($q_\alpha < 0$) term, which is only specified within the reaction layer.

The phase velocities are determined using an extended Darcy's law for multiphase systems [26]:

$$v_\alpha = -\frac{k_{r\alpha}}{\mu_\alpha} K(\mathrm{grad}\, p_\alpha - \rho_\alpha \mathbf{g}), \tag{5}$$

where $k_{r\alpha}$ represents the relative permeability of phase α, μ_α the dynamic viscosity, K the absolute permeability of the porous medium, p_α the pressure of phase α and $\mathbf{g}$ represents the gravity vector. The gravitation effect is neglected by assuming that the gas flow in the channel is downwards, thus the model domain of Fig. 1 corresponds to a horizontal plane.

The capillary pressure represents the discontinuity in pressure that exists across the interface between the two phases when they are in contact in the interstices of a porous medium:

$$p_c = p_g - p_w, \tag{6}$$

where p_g is the pressure in the gas phase and p_w is the pressure in the water phase. Within a capillary tube of radius r, the Laplace equation describes the capillary pressure as

$$p_c = \frac{2\sigma \cos\theta}{r}, \tag{7}$$

where σ is the surface tension and θ is the contact angle. By convention, θ ($0^\circ < \theta < 180^\circ$) is measured through the denser fluid. When $\theta < 90^\circ$, the fluid is said to wet the solid and is called a *wetting fluid*. When $\theta > 90^\circ$, the fluid is called a *non-wetting fluid*.

In the studied system, with a hydrophobic gas diffusion material, the liquid water phase represents the non-wetting phase with $\theta > 90^\circ$ and the gas is the wetting phase, hence the liquid pressure is larger than the gas-phase pressure. The capillary pressure is thus negative.

Eq. (7) also elucidates that, in the case of capillary pressure effects in hydrophobic media, the wetting fluid, i.e., the gas phase, will occupy the smaller pores, whereas the non-wetting fluid, i.e., the water phase, will occupy pores with a larger radius.

In a macroscopic description of porous media a relationship $p_c = p_c(S_w)$ is needed. Hydrophilic media have been intensively investigated in problems of earth sciences and environmental engineering in the last four decades. There are many models which have been obtained from experiments with different soil-like (sandstone) materials. Most commonly used are the Leverett approach [27], the Van Genuchten model [28] and the Brooks and Corey model [29]. They include fitting parameters like a pore-grain-size-form factor and Leverett [27] also includes a temperature dependence through the surface tension and contact angle.

Hydrophobic media have been considerably less investigated. [20,21] used the Leverett approach and included a contact angle >90° to obtain a capillary pressure–saturation relationship for a hydrophobic medium. In our work, we follow another approach. Based on the concept of capillary pressure at the microscale (Eq. (7)), which is widely applied to determine the pore size distribution in any porous medium (e.g., mercury intrusion porosimetry) we obtain the capillary pressure–saturation data that is generated directly during the measurement and correct it for a water–air system considering the differences in surface tension and contact angle. In this way, one obtains a set of data which is comparable with the behaviour of water in the porous carbon material. See Section 4 for a detailed description and the results of this method.

The relative permeability of a phase describes how the presence of one phase influences or disturbs the flow behaviour of the other phase and vice versa. In the earth sciences literature this relationship is commonly derived from the capillary pressure–saturation curve which fits the hydrophilic material data. The most common form of the relative permeability is represented by a cubic function of the saturation. The function $k_{rw}(S_w)$ for the liquid water phase (in a sandstone the wetting phase) is characterized by a slight increase for low saturations and a strong increase for higher saturations. This is due to the fact that, in the case of low saturations, the liquid (wetting fluid) fills only very small pores, where flow movements are nearly impossible because of the strong molecular attraction, whereas the largest pores are only filled in the case of higher saturations.

Because in hydrophobic media the liquid water phase fills first the larger pores, it is expected to obtain a faster increase of the relative permeability of water at low saturations than by hydrophilic media. The reason is that, for lower saturations, the larger pores are filled first, whereas, in the case of almost full saturation, the remaining very small pores, which are filled, have no significant influence on the flow behaviour. For this reason it was decided to derive the relative permeability-saturation relationship from the obtained capillary pressure–saturation data for the present system, as described in Section 4.

For the description of the diffusive component transport in each phase Fick's law is used. For the gas phase it can be used to describe the diffusion of a trace component in a carrier gas, when the interdependencies of the individual mass fluxes of the components can be neglected. Due to the simplicity of Fick's law in describing explicitly the molar diffusive flux of each component, it was decided to make this assumption and to insert the flux term directly into the mass balances. The diffusive flux of each component is thus

$$J_K = -D^K_{\mathrm{pm}} \rho_\alpha \,\mathrm{grad} x^K. \tag{8}$$

D^K_{pm} is the effective macroscopic diffusion coefficient for component K in the porous medium. The effective diffusion coefficient depends on the tortuosity τ, for a multiphase system it also depends on the gas saturation:

$$D^K_{\mathrm{pm}} = \frac{\phi}{\tau} S_{\mathrm{g}} D^K \tag{9}$$

where D^K is the binary diffusion coefficient for the component K in the carrier medium.

A single energy equation is formulated for the fluid-filled porous medium, based on the assumption of local thermal equilibrium in which all phases have the same temperature. In this way heat transport terms between the fluid phases can be neglected. The balance equation can be formulated as follows

$$\begin{aligned}\phi \frac{\partial(\sum_\alpha S_\alpha \rho_\alpha u_\alpha)}{\partial t} + (1-\phi)\frac{\partial \rho_{\mathrm{s}} c_{\mathrm{s}} T}{\partial t} \\ - \mathrm{div}(\lambda_{\mathrm{pm}} \mathrm{grad} T) - \sum_\alpha \mathrm{div}\{k_{\mathrm{r}\alpha} \frac{\rho_\alpha}{\mu_\alpha} h_\alpha K(\mathrm{grad} p_\alpha - \rho_\alpha \mathbf{g})\} \\ - \sum_K \mathrm{div}\{D^K_{\mathrm{pm}} \rho_{\mathrm{g}} h^K_{\mathrm{g}} \mathrm{grad} x^K_{\mathrm{g}}\} - q^{\mathrm{h}} = 0,\end{aligned} \tag{10}$$

where u_α is the internal energy of phase α, c_{s} is the heat capacity of the solid matrix, λ_{pm} is an average thermal conductivity of the fluid filled porous medium, h_α is the enthalpy of phase α and q^{h} represents a heat source or sink.

2.2.2. Electrochemical reaction

The cell potential can be determined by

$$U_{\mathrm{cell}} = U_{\mathrm{oc}} - \eta_{\mathrm{a}} - \eta_{\mathrm{c}} - i R_{\mathrm{spec}}, \tag{11}$$

where U_{oc} is the open circuit voltage (here the reversible cell voltage is used), η_{a} and η_{c} the anodic and cathodic overvoltages, i the current density and R_{spec} is the specific ohmic resistance for the membrane, electrodes and contacts determined experimentally by impedance spectroscopy. These values are listed in Table 3. The anodic overvoltage is neglected in the present work, due to its insignificant contribution.

The transfer overvoltage at the cathode η_{trans} is given using the Tafel kinetics for the oxygen reduction reaction [25]:

$$\begin{aligned}i = i_0^{\mathrm{ref}} f_{\mathrm{v}} \exp\left[\frac{-\Delta G_0^{\neq}}{R}\left(\frac{1}{T} - \frac{1}{T_{\mathrm{ref}}}\right)\right](1-S_{\mathrm{w}}) \frac{p^{\mathrm{O_2}}}{p^{\mathrm{O_2}}_{\mathrm{ref}}} \exp \\ \times \left(\frac{-\alpha z F}{RT}\eta_{\mathrm{trans}}\right),\end{aligned} \tag{12}$$

where i_0^{ref} represents the exchange current density at a reference state, f_{v} a surface increasing factor which describes the relation between the catalytically active and the geometrical surface area of the electrode, $\Delta G_0^{\neq}$ the free activation enthalpy, α the load transfer factor, z the number of transferred electrons per molecule of reactant and F is the Faraday constant. The factor $(1 - S_{\mathrm{w}})$ accounts for the covering effect of the catalyst sites by the liquid phase [15]. $p^{\mathrm{O_2}}$ is the oxygen partial pressure in the reaction layer.

Defining i_0^* as

$$i_0^* = i_0^{\mathrm{ref}} f_{\mathrm{v}} \exp\left[\frac{-\Delta G_0^{\neq}}{R}\left(\frac{1}{T} - \frac{1}{T_{\mathrm{ref}}}\right)\right] \tag{13}$$

and writing Eq. 12 for η_{trans} results in

$$\eta_{\mathrm{trans}} = -\frac{RT}{\alpha z F} \ln \frac{|i|}{|i_0^*|} + \frac{RT}{\alpha z F} \ln \frac{p^{\mathrm{O_2}}}{p^{\mathrm{O_2}}_{\mathrm{ref}}} + \frac{RT}{\alpha z F} \ln(1 - S_{\mathrm{w}}). \tag{14}$$

Moreover, for the space discretization it will be considered that the open circuit voltage at the reaction place, calculated with the local concentration, is not equal to the open circuit voltage at cell inlet, calculated for the cell inlet conditions. This difference, considered as an equilibrium overvoltage η_{equ} [30], is given by

$$\eta_{\mathrm{equ}} = \frac{RT}{zF} \sum_i \nu_i \ln \frac{p^i}{p^i_{\mathrm{inlet}}} = \frac{RT}{zF} \frac{1}{2} \ln \frac{p^{\mathrm{O_2}}}{p^{\mathrm{O_2}}_{\mathrm{inlet}}}, \tag{15}$$

where ν_i are the stoichiometric coefficients of the reacting species in Eq. 2. Now the actual cathodic overpotential is

$$\eta_{\mathrm{c}} = \eta_{\mathrm{trans}} + \eta_{\mathrm{equ}}. \tag{16}$$

Inserting Eq. 14 and 15 in Eq. 11 results:

$$\begin{aligned}U_{\mathrm{cell}} = U_{\mathrm{rev}} - \frac{RT}{\alpha z F}\left(\ln \frac{|i|}{|i_0^*|} - \ln \frac{p^{\mathrm{O_2}}}{p^{\mathrm{O_2}}_{\mathrm{ref}}} - \ln(1 - S_{\mathrm{w}})\right. \\ \left. - \frac{\alpha}{2} \ln \frac{p^{\mathrm{O_2}}}{p^{\mathrm{O_2}}_{\mathrm{inlet}}}\right) - i R_{\mathrm{spec}}.\end{aligned} \tag{17}$$

For a multidimensional case the local current density i for a given constant cell voltage results in an implicit relation:

$$\begin{aligned}i = \frac{1}{R_{\mathrm{spec}}}\left[U_{\mathrm{rev}} - U_{\mathrm{cell}} - \frac{RT}{\alpha z F}\left(\ln \frac{|i|}{|i_0^*|}\right.\right. \\ \left.\left. - \ln \frac{p^{\mathrm{O_2}}}{p^{\mathrm{O_2}}_{\mathrm{ref}}} - \ln(1 - S_{\mathrm{w}}) - \frac{\alpha}{2} \ln \frac{p^{\mathrm{O_2}}}{p^{\mathrm{O_2}}_{\mathrm{inlet}}}\right)\right].\end{aligned} \tag{18}$$

The oxygen consumption rate in the electrochemical reaction is given by Faraday's law:

$$\dot{N}^{\mathrm{R}}_{\mathrm{O_2}} = -\frac{i}{4F}. \tag{19}$$

It is implemented as a (volumetric) sink term in the reaction layer. In the same way, the water production rate is given by

$$\dot{N}^{\mathrm{R}}_{\mathrm{H_2O}} = \frac{i}{2F}. \tag{20}$$

In addition the water flux through the membrane due to electro-osmotic drag is being considered. A water transport number (t_{H_2O}) for a fully hydrated membrane has been assumed (see Table 3):

$$\dot{N}^{M}_{H_2O} = t_{H_2O}\frac{i}{F}. \quad (21)$$

The heat production by the reaction, considered as a heat source, is calculated as

$$\dot{q}^{R} = (U_{th} - U_{cell})i. \quad (22)$$

It is assumed that a part of the heat generated in the cathode reaction layer flows through the membrane to the anode side, depending on the thermal conductivity of the membrane.

2.3. Boundary conditions

Assuming thermodynamic equilibrium and according to the Gibbsian phase rule this non-isothermal system with two phases and three components requires four independent primary variables to be uniquely described. Depending on the phase state of the system at a local point, some variables may need to be switched (see Section 3.2). In this section the initial and boundary conditions are explained assuming that both phases (liquid and gas) are present.

The boundary conditions available in the numerical simulator MUFTE_UG for the Box and CVFE discretization methods (see Section 3) are of types Dirichlet and Neumann (see, e.g., [26]).

The governing equations are identical for both conventional and interdigitated flow fields. The difference exists in the boundary conditions for the primary variables at the interface between the gas channel and the diffusion layer. In all other boundaries, the two types of flow fields have the same boundary conditions.

For $0 \le x \le L$ and $y = 0$ or $y = H$, symmetry conditions are used because $y = 0$ and H correspond to the center of the flow channels (see Fig. 1). Neumann zero boundary conditions are applied (the fluxes of all mass components and the enthalpy flux are set equal to zero).

At the interface with the membrane ($0 \le y \le H$ and $x = 0$) also Neumann zero boundary conditions are taken, because the electrochemical reaction is assumed to occur within the reaction layer thickness. Also the electro-osmotic drag flow of water is for simplicity assumed to occur in the reaction layer, which is described by a source term.

At the interface in contact with the shoulder of the current collector ($H1 \le y \le H2$ and $x = L$) also Neumann zero conditions are applied for all mass components. For the heat term, a constant heat conduction flow is assumed to occur through the shoulder, calculated by

$$q^{shoulder} = \frac{\lambda^{shoulder}}{\delta^{shoulder}}(\Delta T_{cooling}), \quad (23)$$

where $\lambda^{shoulder}$ and $\delta^{shoulder}$ are the thermal conductivity and the thickness of the shoulder, respectively.

2.3.1. Conventional gas distributor

For $H2 \le y \le H$ and $0 \le y \le H1$ and $x = L$ (i.e., at the inlet of the reacting gases) Dirichlet boundary conditions for oxygen concentration in the gas phase, liquid water saturation, total gas pressure and temperature are set:

$$x_g^{O_2} = x_g^{O_2,inlet}, \quad S_w = 0, \quad p_g = p_g^{inlet}, \quad T = T^{inlet} \quad (24)$$

In this work, treating hydrophobic materials it is for simplicity assumed that the liquid water saturation at the channel interface is near to zero. In the real operation, depending on the actual wettability of the gas diffusion material and on the water vapor content of the gas stream, a specific value is expected to be established. One approach to estimate this saturation value at the interface could be obtained from a local equilibrium assumption, based on sorption/desorption isotherms determined experimentally for these materials under different operating conditions of water vapor saturation in the gas phase. This is out of the scope of the present work and should be studied in further investigations.

2.3.2. Interdigitated gas distributor

For $H2 \le y \le H$ and $x = L$ (flow inlet) Neumann fluxes of all mass components are set. For the energy equation a Dirichlet condition for the inlet temperature is used.

For $0 \le y \le H1$ and $x = L$ (flow outlet) the fluid phases can break through into the gas channel at the outlet pressure p_g^{outlet}. The difficulty in the modeling arises from the fact that this boundary cannot be described correctly by either a Dirichlet or a Neumann boundary condition. Instead, we had to choose a modified model domain that allows a quasi-simulation of the conditions at the outlet in the gas channel. We extended the domain in the horizontal direction as shown in Fig. 2. At the new boundary ($0 \le y \le H1$ and $x = L_{extension}$) a liquid water saturation of zero was assumed. We assigned to this extended portion high flow properties (permeability) in order to make sure that the outlet of the diffusion layer is influenced only minimally by the righter Dirichlet condition for the water saturation. For the oxygen transport, it is assumed that the gas is completely mixed in the outlet channel at the interface with the gas diffusion layer ($0 \le y \le H1$ and $x = L$). At the outlet of the extended portion ($0 \le y \le H1$ and $x = L_{extension}$) the diffusion term is eliminated, to make sure that back-diffusion has no influence on the real model domain.

For the energy equation, a free boundary for the enthalpy flow is chosen at ($0 \le y \le H1$ and $x = L$), so that the heat flux is allowed out of the domain as it occurs due to the respective gradient given at the boundary.

3. Numerical solution technique

The system of flow and transport equations as explained in the previous sections puts a high demand on the numerical solution techniques. The resulting system of partial differential equations is highly coupled and non-linear. The equations are of a mixed hyperbolic and parabolic character with a varying dominance depending on the influences of capillary pressure and the ratio of convective to diffusive fluxes. The equations have been implemented into the numerical simulator MUFTE_UG

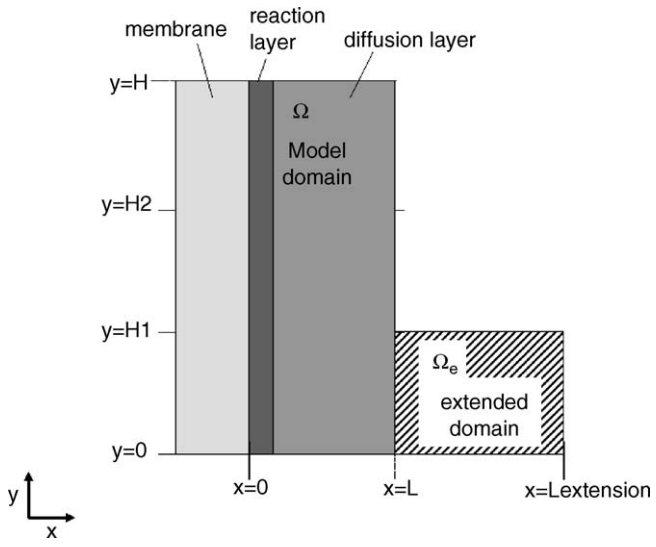

Fig. 2. Extended two-dimensional model domain.

[31] which was developed as a research code for multiphase flow in porous media. The model domain shown in Fig. 1 is, after multigrid refinement, divided into 6400 equally sized rectangular grid cells. There are 40 divisions in x-direction and 160 divisions in y-direction.

3.1. The numerical simulator MUFTE_UG

MUFTE_UG is a sophisticated numerical tool that is continuously developed in a joint-venture project of the Interdisciplinary Center for Scientific Computing, University of Heidelberg, (part: UG) and the Institute of Hydraulic Research, University of Stuttgart (part: MUFTE). The toolbox UG, standing for Unstructured Grids, is the developing platform. It provides a number of powerful numerical algorithms for solving systems of partial differential equations on unstructured grids, cf. [32] or [33]. MUFTE stands for multiphase flow transport and energy model. It can be applied to simulate isothermal and non-isothermal multiphase multicomponent flow in porous and heterogeneous or fractured media. MUFTE contains the problem-specific implementation of the equations, including discretization methods, constitutive relationships, and boundary conditions. Both UG and MUFTE have strictly modular structure allowing the combination of different problem classes with various numerical solution methods. A good overview of the available model concepts and algorithms is given, for example, by Helmig [26] or Class et al. [34].

3.2. Adaptive choice of the primary variables

The non-isothermal system of the two phases gas and water including the three mass components water, oxygen and nitrogen is described by the mass balance equations and the thermal energy equation as explained in Section 2.2.1. Depending on the number of phases locally present in a control volume different phase states are distinguished. For this work, two relevant phase states are the state 'both phases' and the state with only the gas phase present. If both phases exist, water saturation S_w, gas-phase pressure p_g, temperature T, and oxygen mole fraction in the gas-phase $x_g^{O_2}$ are chosen as the primary variables. A single-phase gas state requires a switching of the primary variable saturation to an additional gas-phase mole fraction. The switching algorithm and further details can be found in [34].

3.3. Box discretization

Eqs. (4) and (10) are spatially discretized with the so-called Box method, which represents a strictly mass-conservative Subdomain Collocation Method, cf. [26]. The Box method requires the construction of a secondary mesh. This is achieved by connecting the centers of gravity of the elements with the mid-points of the element edges. By this each node is assigned an unique control volume. On the other hand, each element contains a number of sub-control volumes equal to the number of nodes. The discretization scheme can be derived using the principle of weighted residuals applied on the primary finite element mesh with piece-wise constant weighting functions for the control volumes (boxes) on the secondary mesh. We apply a mass lumping for avoiding non-physical oscillations of the solution. The advective terms in the equations are computed with a fully upwind technique. This implies an upstream evaluation of mobilities, mole fractions and enthalpies.

3.4. Time-step procedure and solution methods

The system of partial differential equations resulting from Eqs. (4) and (10) is highly non-linear. It is linearized using a damped in-exact Newton-Raphson method, as described in [35].

For the time discretization we use a fully implicit Euler scheme applied to the storage terms. We use here a stabilized bi-conjugated gradient method (Bi-CGStab) optionally with an extended multigrid preconditioner, cf. [33,34] as linear solver for the Jacobian system.

4. Parameter determination

Properties of the commercial GDL material Double Sided ELAT from E-TEK, Inc., needed in the model are determined experimentally. These are described in the following. For illustration purposes some SEM photographs of the top and a cross section of an ELAT electrode are shown in Figs. 3–5, respectively.

4.1. Contact angle

The wetting properties of the gas diffusion material ELAT–DS were investigated by measuring the contact angle with the sessile drop method [36,37]. Two different samples of the material from the same production batch are cut out with a size of 50 mm × 50 mm. The contact angle is measured at three different positions on each sample. To measure the contact angle a droplet of deionised water with 3 mm diameter is placed on the surface of the sample. Then a picture from the side is taken with

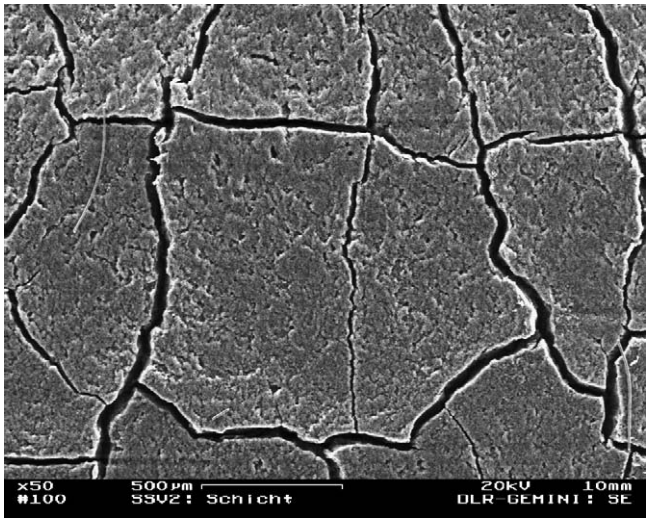

Fig. 3. SEM micrograph of an ELAT–DS electrode – top view – 50× magnification.

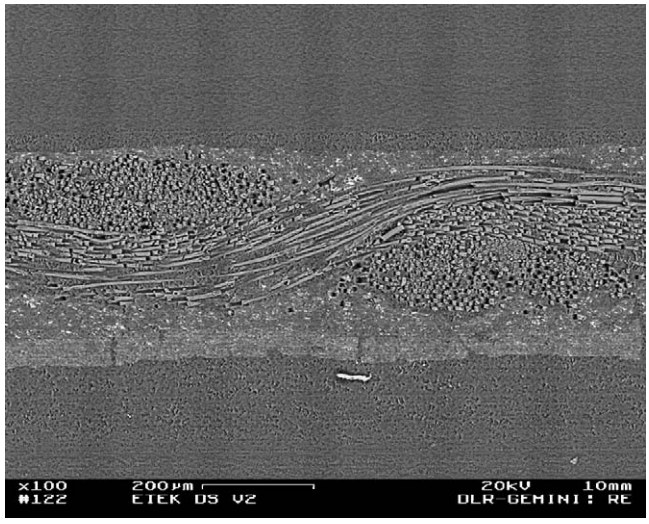

Fig. 5. SEM micrograph of an ELAT–DS electrode – cross-section – 100× magnification.

a CCD camera [36]. The image is analyzed using the Software DSA1 v.1.80 Drop Shape Analysis from Krüss GmbH, which calculates the contact angle by fitting a tangent on the drop profile at the three-phase point where the liquid surface contacts the solid surface. For the ELAT–DS gas diffusion layer the measured contact angle for water is 143° with a standard deviation of 2°. For mercury the contact angle has a value of 141° on the ELAT–DS electrode.

4.2. Porosity

The pore size distribution of the investigated gas diffusion material ELAT–DS is measured by mercury intrusion porosimetry [38] using a Pascal 240 Porosimeter from Porotec GmbH. This method forces mercury with its high surface tension to penetrate the pores of the gas diffusion layer. Setting the amount of mercury uptake as a function of pressure, allows for the determination of the pore size distribution. The results of the measured pore size distribution are shown in Fig. 6.

To calculate the porosity, the thickness of the sample is determined via SEM. For ELAT–DS a thickness of 0.45 mm was obtained. The resulting porosity of ELAT–DS is 78%.

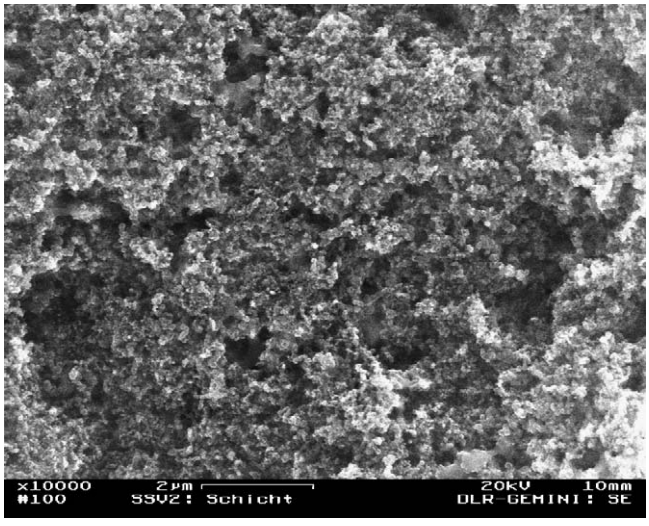

Fig. 4. SEM micrograph of an ELAT–DS electrode – top view – 10 000× magnification.

4.3. Tortuosity

The Wicke–Kallenbach diffusion cell [39] allows for the investigation of the diffusivity of dry gases through the gas diffusion material. The diffusion cell consists of two chambers, which are separated by the investigated gas diffusion layer ELAT–DS. The pressure difference between the chambers is set to zero. Well-defined gas flows through each chamber pass the surface of the investigated gas diffusion layer. With a gas chromatograph each gas flow composition is measured at the inlet and outlet of the diffusion cell to determine the diffusive fluxes through the gas diffusion layer. The effective diffusivity

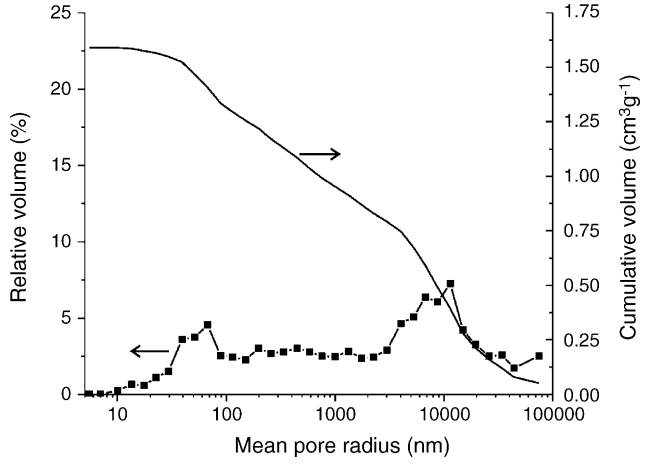

Fig. 6. Pore size distribution of ELAT–DS electrode.

is related to the binary diffusion coefficient by

$$D_{\text{eff}} = \frac{\phi}{\tau} D_{ij}. \tag{25}$$

Combining D_{eff} from the Wicke–Kallenbach experiment and the porosity ϕ measured by mercury intrusion porosimetry, an experimentally determined value for the tortuosity τ is obtained from the above equation. The tortuosity comprises all factors inhibiting species transport within the dry porous diffusion layer, such as indirections and dead-end pores. The measured effective diffusion coefficient of H_2 in nitrogen is $5.533 \times 10^{-6} \pm 1.019 \times 10^{-6}\,\text{m}^2\,\text{s}^{-1}$. The effective diffusion coefficient for O_2 in nitrogen is $1.91 \times 10^{-6} \pm 0.68 \times 10^{-6}\,\text{m}^2\,\text{s}^{-1}$. The errors in the effective diffusion coefficient are mainly due to the quality of the calibration gases for the gas chromatograph (uncertainty in the exact concentration). Therefore, the calculated tortuosity of ELAT–DS is 3 ± 1.

4.4. Capillary pressure

For the determination of the capillary pressure–saturation relationship the mercury injection porosimetry method was also applied. Mercury is normally a non-wetting fluid. The core is placed in a chamber, which is then evacuated to a very low pressure, and mercury is forced into the core under pressure, as already mentioned in Section 4.2. The volume of mercury injected at each pressure determines the non-wetting fluid saturation (taking into account the volume of the cell and the bulk volume of the sample). The rest gas represents the wetting phase. The procedure is continued until the core sample is saturated with mercury, or pressure reaches a predetermined value. Applying a correction permits to obtain the values for a water–air system, taking into account the different surface tension and contact angle, as proposed in [38,40]:

$$\frac{p_{\text{c water–air}}}{p_{\text{c Hg–air}}} = \frac{\sigma_{\text{water}} \cos\theta_{\text{water}}}{\sigma_{\text{Hg}} \cos\theta_{\text{Hg}}}. \tag{26}$$

Fig. 7 shows the obtained corrected data for a water-air system for the ELAT–DS sample, with a zoom for the region of low capillary pressures.

The hysteresis typical for the drainage and imbibition processes is clearly shown in Fig. 7. As one can observe, during the drainage process the liquid is held back in the pores of the sample, yielding a higher liquid phase saturation. At the end of the drainage measurement, a liquid amount is still present in the sample, which represents the residual saturation.

It should be mentioned that the terms “imbibition” and “drainage” will be used throughout this contribution in their colloquial meaning, namely imbibition for water uptake and drainage for de-watering. This is in contrast to literature where drainage is often defined as the replacement of the wetting fluid (here air) through the non-wetting fluid (here water). Since the electrode materials studied have both hydrophobic and hydrophilic properties which is discussed below, the literature definition would lead to confusion if the material properties change between wetting and non-wetting. Given the capillary pressure vs. saturation curve of Fig. 7, two points need to be discussed:

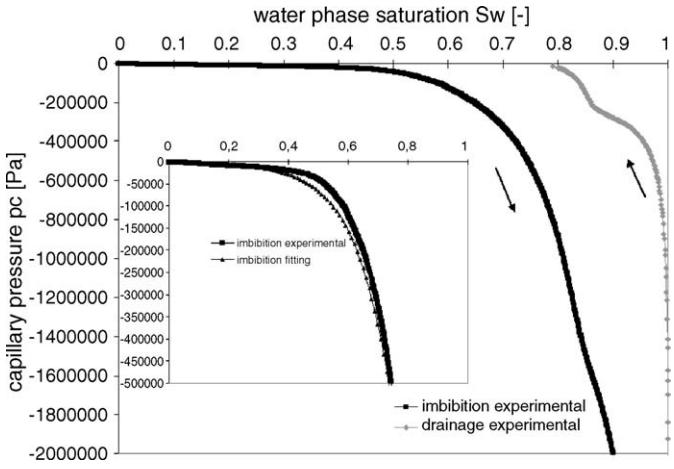

Fig. 7. Capillary pressure–saturation data for DS–ELAT electrode corrected for a water-air system. The insert shows the relevant range of capillary pressure and a fitting for the imbibition curve.

(1) Which curve, imbibition or drainage from Fig. 7 should be used for the simulation?
(2) It is well known that any electrode material is not completely hydrophobic but takes up a certain amount of water at zero (capillary) pressure, whereas mercury is completely unwetting. The conversion of the mercury porosimetry data to water using Eq. (7) does not take this difference into account. The imbibition or drainage curves for water will therefore in reality not level off at zero saturation as in Fig. 7 but extend into positive capillary pressures as in Fig. 8.

Since at present no detailed experimental studies of these effects are available, we will in the following consider two limiting cases. The first case is the completely unwetting behaviour, characterized by the imbibition curve fitted to Fig. 7. The second case is the (more realistic) case of partial wetting, assuming the fit to the drainage curve of Fig. 8 with an extension at low saturation into positive capillary pressure.

For the parametrization of the imbibition curve the following equation has been used

$$p_{\text{c}} = A_1 \exp(B_1 S_{\text{w}} + C_1) + D_1(1 - S_{\text{w}}). \tag{27}$$

For the drainage process, further measurements with water have to be made in order to obtain the missing data at low saturations. In this work, following equation has been used:

$$p_{\text{c}} = A_2 \exp(B_2 S_{\text{w}} + C_2) + D_2(1 - S_{\text{w}}) + \frac{E_2}{S_{\text{w}}}, \tag{28}$$

which is shown in Fig. 8 together with the experimental values.

4.5. Permeability

4.5.1. Absolute permeability

The absolute or intrinsic permeability is a parameter characterizing only the porous medium, it is independent of the fluid or fluids present. For the determination of the absolute through-plane permeability of the porous electrode material an annulus-shaped GDL sample was situated between two plates

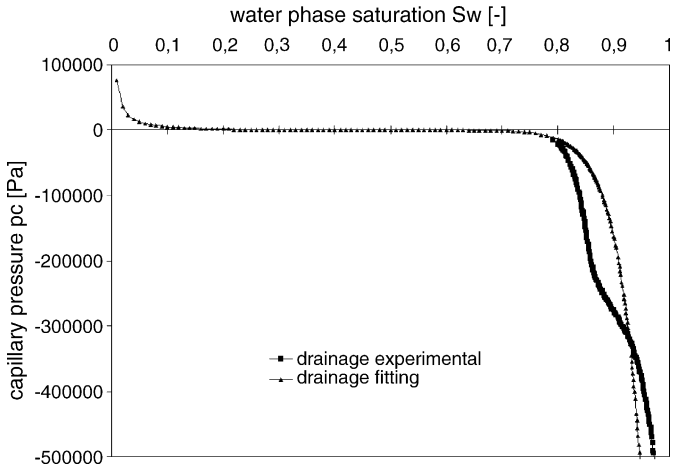

Fig. 8. Capillary pressure–saturation drainage data and fitting curve for DS–ELAT electrode.

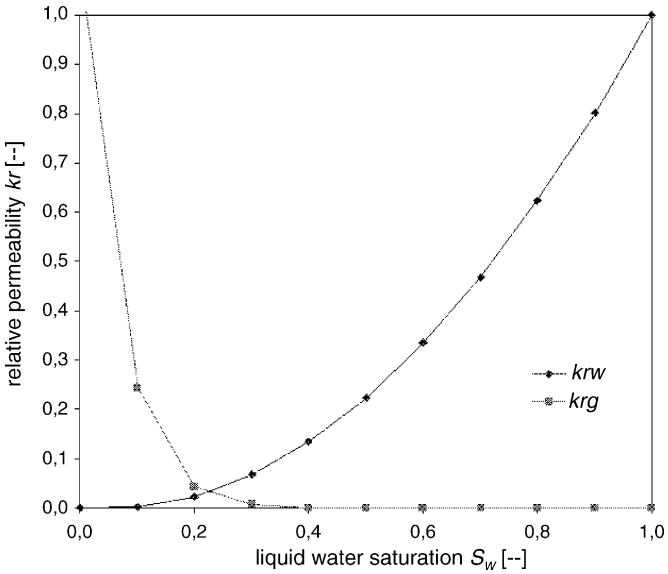

Fig. 9. Relative permeability curves obtained for the DS–ELAT electrode.

of a metallic cell. Dry air was fed to the cell at a controlled rate, and the pressure loss between gas inlet and outlet was measured with a manometer (Bexbill England FCO12-Micromanometer). The through-plane permeability for the investigated ELAT–DS material was determined as $5.20 \times 10^{-11}\,\mathrm{m}^2$, which is a little lower than the permeability for a sandstone (approximately $\times 10^{-10}\,\mathrm{m}^2$) but is in the range of other commercial GDL materials as reported by Ihonen et al. [22].

4.5.2. Relative permeability

As mentioned in Section 2.2.1 the relative permeability accounts for the interaction of one phase on the flow behaviour of the other. In a continuum approach it is a dimensionless number between 0 and 1, which depends on the phase saturation. There are several proposed methods for the determination of the relative permeability–saturation relationship $k_{\mathrm{rw}}(S_{\mathrm{w}})$ from the capillary pressure data, see e.g., [41] for a detailed explanation of the different models. In the present work we assumed a capillary pore model of parallel tubes with constant cross-section in flow direction and the Burdine [42] approach for the tortuosity dependency on the saturation, resulting in

$$k_{\mathrm{rw}} = \left[\frac{S_{\mathrm{w}} - S_{\mathrm{wr}}}{1 - S_{\mathrm{wr}}}\right]^2 \frac{\int_0^{S_{\mathrm{w}}} \frac{\mathrm{d}S_{\mathrm{w}}}{p_{\mathrm{c}}^2}}{\int_0^1 \frac{\mathrm{d}S_{\mathrm{w}}}{p_{\mathrm{c}}^2}}, \tag{29}$$

$$k_{\mathrm{rg}} = \left[1 - \frac{S_{\mathrm{w}} - S_{\mathrm{wr}}}{1 - S_{\mathrm{wr}}}\right]^2 \frac{\int_{S_{\mathrm{w}}}^1 \frac{\mathrm{d}S_{\mathrm{w}}}{p_{\mathrm{c}}^2}}{\int_0^1 \frac{\mathrm{d}S_{\mathrm{w}}}{p_{\mathrm{c}}^2}}. \tag{30}$$

S_{wr} is called the *residual saturation* of the water phase. It represents the amount of fluid under which no phase continuity exists anymore and the phase is considered immovable. Fig. 9 shows the obtained curves for the relative permeability of each phase using the imbibition data.

Note that $k_{\mathrm{rw}} + k_{\mathrm{rg}} < 1$ due to the pore space connectivity, by which the flow paths are interconnected and the phases interfere each other.

5. Results and discussion

The model was used to evaluate the influence of the flow configuration and capillary properties of the diffusion layer material on the cell behaviour. In the following the results for the imbibition curve are shown both using conventional and interdigitated type gas distributors. Furthermore, calculations using the extended drainage curve from Fig. 8 are performed. It should be noted that this two-dimensional model is limited to the channel entrance of the fuel cell and can not take into account the three-dimensional effects that originate along the channels.

5.1. Imbibition curve results

Tables 1–4 list the parameter values used for the calculations. As is shown, the air is assumed to be completely humidified with water vapor but no liquid water is present at the channel interface. The dimensions of the channel and shoulder heights for the gas distributor correspond to the dimensions used in our fuel cell with an active area of $25\,\mathrm{cm}^2$. For the cell voltage, a value of 0.5 V is used. Other conditions and parameters used in the study are shown in these tables along with the references for various parameters used in the model.

Table 1
Geometrical and gas distributor parameters

Geometrical parameters	
Length, x (L) (cm)	0.05
Length, y (H) (cm)	0.2
Gas distributor parameters	
Channel width (half) (cm)	0.05
Shoulder width (cm)	0.1
Thermal conductivity, $\lambda^{\mathrm{shoulder}}$ ($\mathrm{W\,K^{-1}\,m^{-1}}$)	14.7
Flow field plate thickness, $\delta^{\mathrm{shoulder}}$ (cm)	0.3
ΔT for cooling (K)	2

Table 2
Electrode parameters

Diffusion layer parameters	
Diffusion layer thickness (cm)	0.045
Porosity, ϕ	0.78
Absolute permeability, K ($\times 10^{-11}$)	5.20
Residual water saturation for imbibition process, S_{wr}	0.05
Residual water saturation for drainage process, S_{wr}	0.41
Contact angle water, θ_{water} (°)	143
Contact angle mercury, θ_{Hg} (°)	141
Surface tension of water, σ_{water} (N m^{-1})	0.0625
Surface tension of mercury, σ_{Hg} (N m^{-1})	0.480
Constants used in capillary pressure–saturation	
A_1, B_1, C_1, D_1 (Eq. (27))	−1168.75, 8.5, −0.2, −700
A_2, B_2, C_2, D_2, E_2 (Eq. (28))	−600, 25, −16, −3300, 800
Tortuosity, τ	3
Thermal conductivity, λ [25] (W K^{-1} m^{-1})	15.6
Heat capacity, c_p [25] (J kg^{-1} K^{-1})	710
Reaction layer parameters	
Reaction layer thickness [25] (cm)	0.005
Porosity, ϕ [25]	0.07
Tortuosity, τ [25]	5

Table 3
Parameters for the electrochemical reaction

Reversible voltage at $T = 70$ °C, U_{rev} (V)	1.191
Thermoneutral voltage at $T = 70$ °C, U_{th} (V)	1.4836
Free activation enthalpy [43], $\Delta G_0^{\neq}$ ($\times 10^3$ J mol^{-1})	73.0
Cell voltage (V)	0.5
Exchange current density ORR i_o^{ref} [43] ($\times 10^{-8}$ A cm^{-2})	1.87
Reference temperature [43] (K)	353.15
Reference partial pressure of O_2 [43] ($\times 10^5$ Pa)	5.0
Transfer coefficient for oxygen reduction, α [25]	0.5
Surface increasing factor, f_v [25]	60
Electro-osmotic drag coefficient, t_{H_2O} [44]	0.2327
MEA specific resistance R_{spec} [25] (Ω m^2)	0.25
Membrane thermal conductivity, λ^M [45] (W K^{-1} m^{-1})	0.43
Membrane thickness, δ^M (μm)	87.5

5.1.1. Conventional flow field

For the conventional flow field, the gas stream flows parallel to the diffusion layer and the oxygen transport mechanism to the reaction layer is represented by diffusion. Fig. 10 provides the steady-state concentration profiles of oxygen, liquid water saturation and temperature distribution for the imbibition curve. Fig. 11 shows the local current density profile along the electrode height at the interface membrane/catalyst layer.

At the channel/diffusion layer interface, the oxygen concentration is set to inlet boundary condition that is a mole fraction of 0.1775 for oxygen in air saturated with water vapor at the inlet temperature of 70 °C and pressure of 2 bar. From this interface oxygen diffuses to the reactive surface through the porous gas diffusion layer where it is consumed by the electrochemical reaction to produce water. Also the water flow coupled to the proton transport through the membrane coming from the anode side is accounted for at the reaction layer. The water accumulated at the cathode is removed in general by two mechanisms, i.e., capillary flow and evaporation. In this case, the air flow is completely saturated with water vapor, so that capillary action represents the dominant mechanism.

Table 4
Operational conditions

Inlet gas pressure ($\times 10^5$ Pa (abs))	2.013
Inlet gas temperature (°C)	70
Inlet oxygen mole fraction	0.1775
Inlet water vapor mole fraction	0.1546
Inlet liquid water saturation	0.01
Inlet stream relative humidity (%)	100

In the reactive regions under the channels, the reactants and products need to cover only the thickness of the diffusion layer, therefore mass transport is fast. Otherwise, in the reactive region under the shoulder, the reactants and products have to diffuse across the thickness and height of the diffusion layer. Hence, a lower availability of oxygen and a greater accumulation of water in the diffusion layer under the shoulder is expected as can clearly be seen in the oxygen mole fraction and liquid water saturation distribution profiles in Fig. 10. Since the current density along the electrode length is directly affected by the oxygen availability, the current density profile shown in Fig. 11 matches the oxygen profile in the catalyst layer. The air cathode average current density for the whole reaction layer for the imbibition curve using conventional gas distributors is calculated to be 0.69 A cm^{-2}.

The liquid water saturation in the cathodic GDL is higher in the region under the shoulder and increases only up to 11.5 %. This is because the liquid water generated under the shoulder accumulates there despite the lower rate of water generation in this region. Due to the longer distance to the channel in the region under the shoulder, the liquid water can not be removed as quickly as in the region directly under the channels. The liquid water flux, induced by the gradient in the liquid water saturation, is directed from the catalyst layer into the channel, i.e., in the opposite direction to the gas phase (diffusion) flux.

From the temperature profile (Fig. 10(c)) one can see that the temperature is also higher in the region of high current densities, that is the reaction zone under the channels. This is because the shoulder is cooled by heat conduction into the current collector. The small temperature increase within the GDL depends on the thermal conductivity of the material and is in agreement with other simulation studies, e.g., [12].

5.1.2. Interdigitated flow field

When an interdigitated gas distributor is used, oxygen and water are transported to and from the inner layer of the electrode by both, diffusion and convection induced by the pressure drop created between the inlet and outlet channels. This convective flow through the electrode reduces the gas diffusion distance to and from the catalyst layer, and by having gas flowing under the shoulders of the gas distributor, the electrode active area under the shoulder is better utilized [13]. Also, the liquid water removal is enhanced, thereby reducing the electrode flooding problems. These benefits help to extend the cell operable conditions to higher current densities and consequently higher power densities.

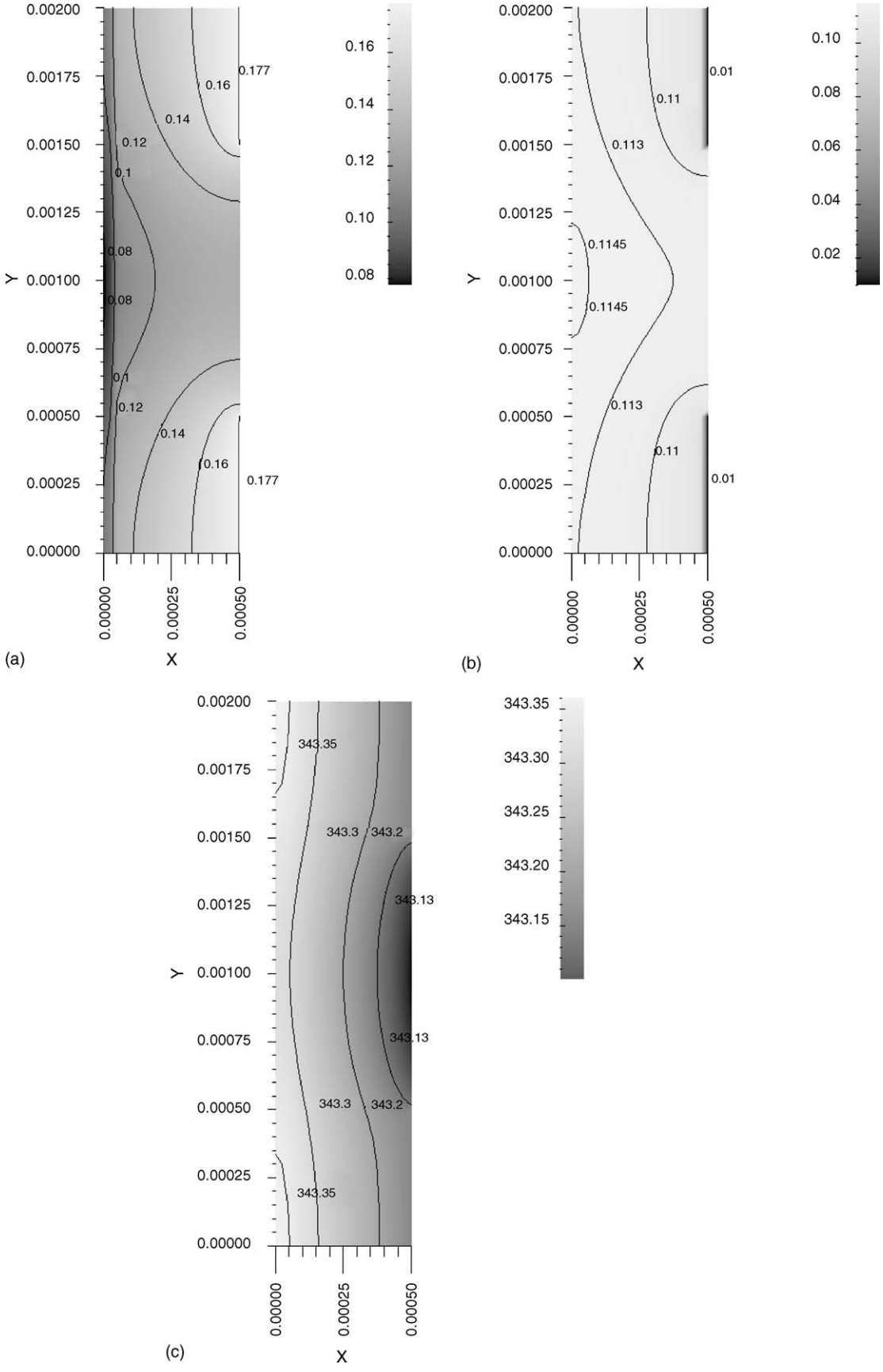

Fig. 10. Oxygen concentration, $x_g^{O_2}$ (a), liquid water saturation, S_w (b) and temperature, T (K) (c) distribution in the electrode for the imbibition curve—conventional gas distributor (X, electrode thickness and Y, electrode height).

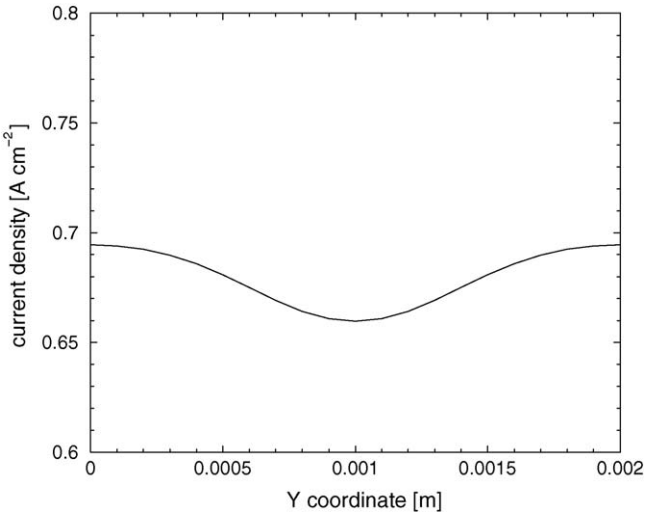

Fig. 11. Current density distribution at the catalyst layer–membrane interface for the imbibition curve—conventional gas distributor.

The results are given in Figs. 12–14. Like for the conventional gas distributor, the inlet gas stream is assumed to be completely saturated with water vapor, but no liquid water is present in the channel. The reactant fluxes were taken for an air stoichiometric flow rate of 2 at 1 A cm^{-2}. The gas inlet temperature is set to 70 °C and the gas backpressure is set to 2 bar.

Fig. 12 shows the pressure distribution and the gas velocity within the electrode. At the inlet, the *x*-direction velocity is high and quickly decreases and transfers its momentum to the *y*-direction velocity. The same occurs at the outlet where the *y*-direction velocity decreases and transfers the momentum to the *x*-direction velocity. These velocities peak near the inlet/shoulder and outlet/shoulder corners because they constitute the shortest distance between the inlet and outlet channels.

Fig. 13 shows the oxygen concentration, liquid water saturation and temperature distribution profiles within the electrode. Fig. 14 shows the local current density profile along the electrode height at the interface membrane/catalyst layer.

The oxygen mole fraction is highest in the inlet region ($0.0015\,\text{m} \leq y \leq 0.002\,\text{m}$). From there, the oxygen concentration decreases as oxygen moves from the inlet toward the catalyst layer, where it is consumed as shown in Fig. 13(a). The oxygen mole fraction within the electrode layer continues to decrease along the *y*-direction as oxygen is continuously consumed along the catalyst layer. Water is generated within the catalyst layer, the electro-osmotic water flow, which depends on the reaction rate, is also assumed to appear within the thin catalyst layer. The liquid water saturation shown in Fig. 13(b) is some higher in the region under the shoulder but is almost uniform within the electrode. The maximum liquid water saturation for this case is about 8% and thus a little lower as the value obtained for the conventional gas distributor. The current

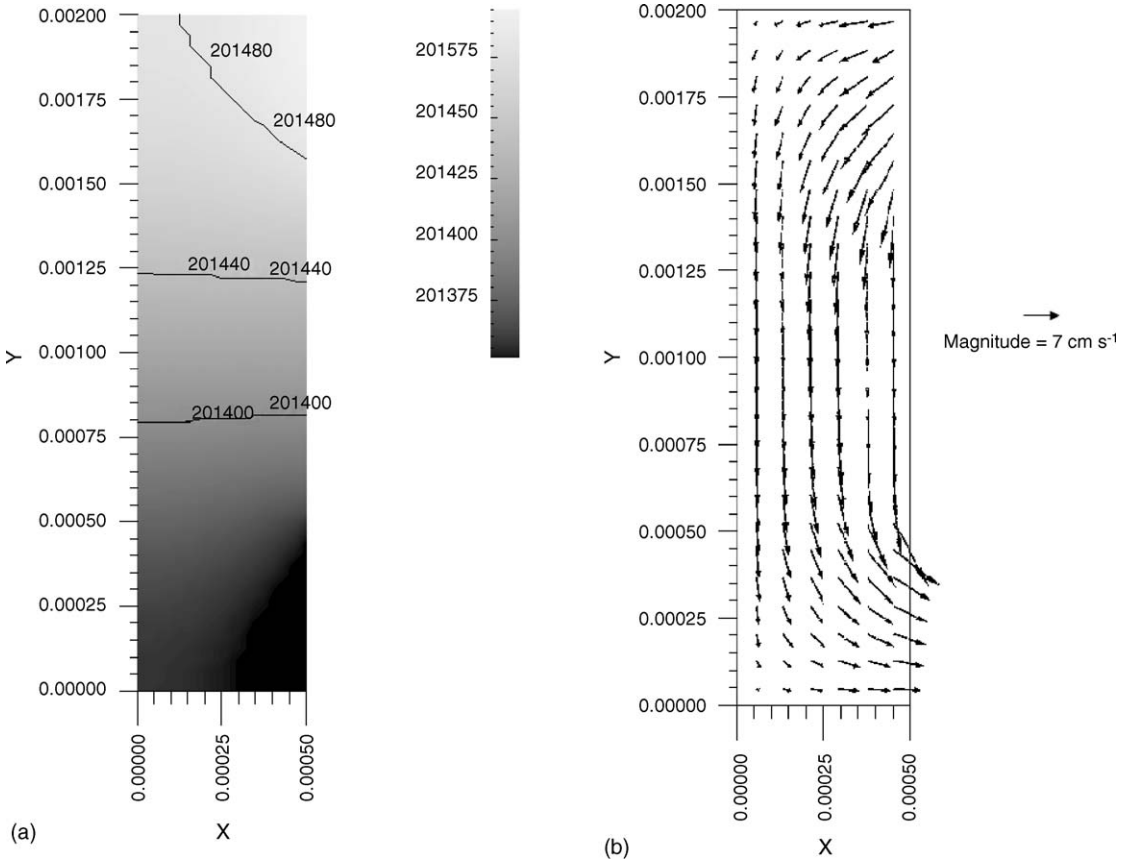

Fig. 12. Gas pressure distribution and vector plot of the gas velocity in the electrode for the imbibition curve—interdigitated gas distributor (*X*, electrode thickness and *Y*, electrode height): (a) p_g (Pa); (b) v_g (m s^{-1}).

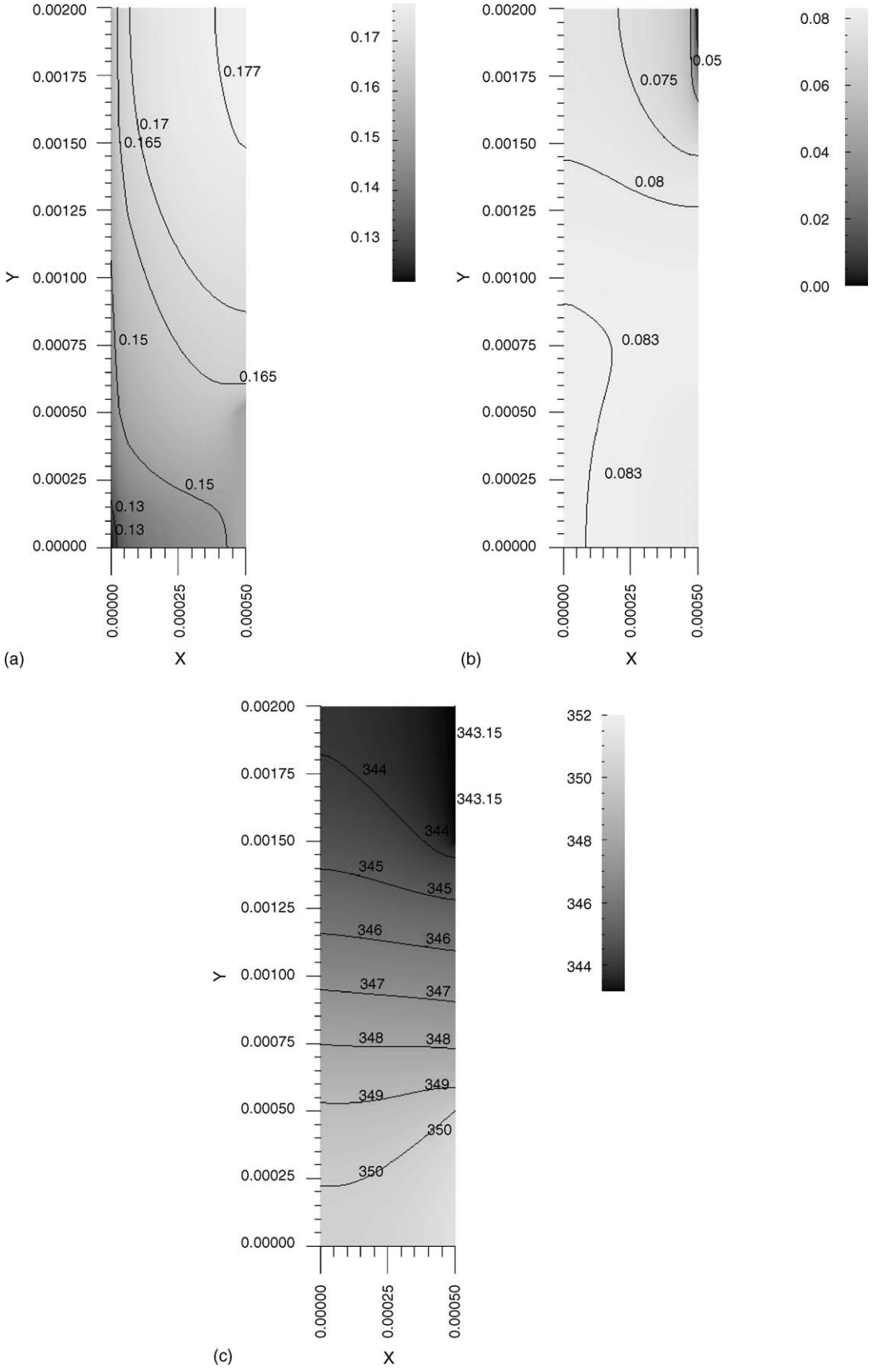

Fig. 13. Oxygen concentration, $x_g^{O_2}$ (a), liquid water saturation, S_w (b) and temperature, T (K) (c) profiles in the electrode for the imbibition curve—interdigitated gas distributor (X, electrode thickness and Y, electrode height).

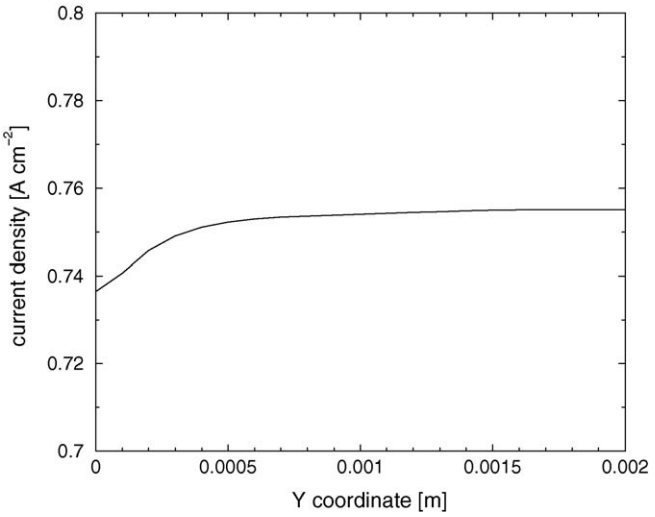

Fig. 14. Current density distribution at the catalyst layer–membrane interface for the imbibition curve—interdigitated gas distributor.

density profile, Fig. 14, corresponds to the oxygen profile along the interface to the catalyst layer as shown in Fig. 13(a). The average current density for the imbibition curve using interdigitated gas distributors for a cell voltage of 0.5 mV is calculated to be 0.75 A cm^{-2}.

The temperature profile (Fig. 13(c)) is in the same way different from the conventional gas distributor. In this case, the gas temperature increases throughout the electrode due to the reaction enthalpy and reaches the maximum value at the outlet in spite of the cooling through the shoulder. The cooling flow (considered for simplicity as constant) is for this case not high enough to reduce the temperature of the outflowing gas stream. For this reason, a higher temperature increase is observed for this gas distributor.

When comparing the results for both gas distributors using the imbibition curve, one can observe a lower liquid water saturation within the electrode when the interdigitated flow field is used. Due to the faster oxygen transport by convection, the oxygen mole fraction and thus the current density are also higher for this type of flow distributor. At an overvoltage of

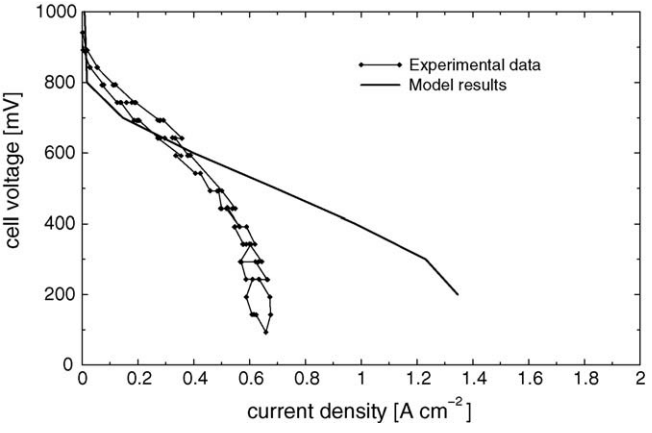

Fig. 15. Imbibition curve results and measured polarization curves for the conventional gas distributor operating with air.

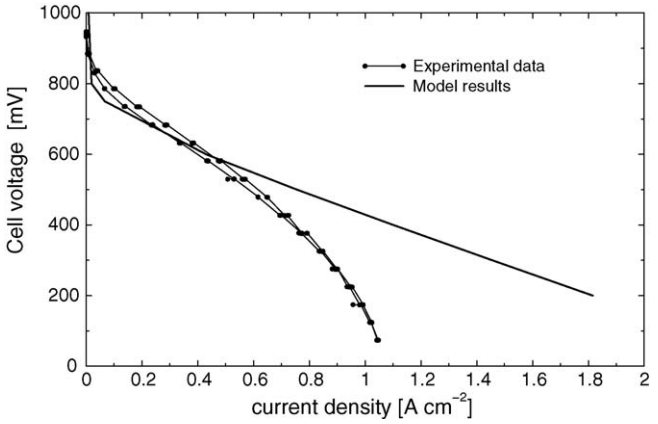

Fig. 16. Imbibition curve results and measured polarization curves for the interdigitated gas distributor operating with air.

200 mV the current density reaches a value of 1.36 A cm^{-2} for the conventional gas distributor and 1.82 A cm^{-2} for the interdigitated one. However, e.g., Nguyen et al. [13] and Kazim et al. [7] report much higher current density values for the interdigitated gas distributors. This is due to the fact that they assume much higher values for the pressure drop between inlet and outlet channels, as Nguyen et al. [13] observed from their experiments.

In our model, at the inlet boundary we assume the Neumann fluxes for the reactant species so that the pressure drop is calculated. The obtained value of about 160 Pa is much lower than the value reported by He et al. [13] and Kazim et al. [7], for example, that is in the range of 700 Pa. In our cell laboratory measurements, we also observe higher pressure drops than predicted by our model, but this pressure drop varies significantly depending on the humidity of the gas stream and the current density, i.e., the amount of liquid water present in the cathode, as also reported by He et al. [46] and Thoben and Siebke [47]. Because the liquid water saturation distribution is a variable being calculated for the GDL, we preferred to set the values for the fluxes and the gas backpressure rather than the pressure drop at the electrode.

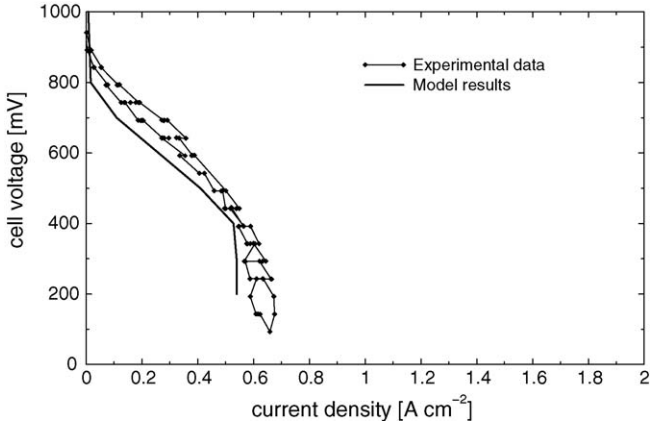

Fig. 17. Simulated polarization curve for a partially hydrophilic electrode, drainage curve, and ELAT–DS measured curve for comparison—conventional gas distributor operating with air.

The low value obtained for the pressure drop indicates that in practice higher liquid water saturations are to be expected in the GDL. This effect can not be reproduced by the imbibition curve in Fig. 7. Also the assumption of zero water saturation at the channel interface through the boundary condition has to be more adequately formulated based upon measurements of the equilibrium uptake of water (water saturation) depending on water vapour partial pressure. Moreover, this two-dimensional model cannot account for the water accumulation along the channels.

5.2. Comparison with experimental data

The model results are compared to a set of experimental data collected on a 25 cm^2 cell both with a conventional gas distributor and with an interdigitated gas distributor. A Nafion 1135 membrane (DuPont) was placed between two electrodes of type Double Sided ELAT from E-TEK, Inc., with a Pt loading of 1.0 mg Pt cm^{-2} (20% Pt on Vulcan XC-72) and impregnated with Nafion solution with a loading of approx. 1.5 mg Nafion cm^{-2}. Before the installation in the test facility, the MEA was hot pressed [48]. The polarization curve for this MEA was generated using a single-cell assembly, with a conventional flow field at the anode side and, respectively, an interdigitated and a conventional flow field for the cathode. The cell was operated at 70 °C, the anode and cathode stream were humidified with a sparging bottle held at 80 °C. Hydrogen was supplied to the anode and air to the cathode at a stoichiometric flow rate of 1.5 and 2 at 1 A cm^{-2}, respectively. Both gases had a pressure of 2 bar.

Figs. 15 and 16 show, respectively, the experimental results for the conventional and the interdigitated gas distributor, and the model results using the imbibition curve from Fig. 7 (Insert). In both diagrams one can identify two different effects. At high cell potentials, over 700 mV, the predicted current densities are slightly lower than the measured values. The reason for the deviations may be inaccuracies in rate constants of the electrochemical reactions in this kinetic limited region. At cell voltages below 600 mV, where transport limitations become significant, the model predictions for the current density become significantly higher than the experimental values. That is attributed to the low liquid water saturation values predicted by the model by assuming a completely hydrophobic material. In practice, the gas diffusion layer material is only partially hydrophobic, and can also turn more hydrophilic under cell operation, as also reported by Reissner et al. [49].

However, as shown in both Figs. 15 and 16, the simulation results predict the improvement in cell performance with the interdigitated gas distributor correctly, showing a higher limiting current density for this flow configuration.

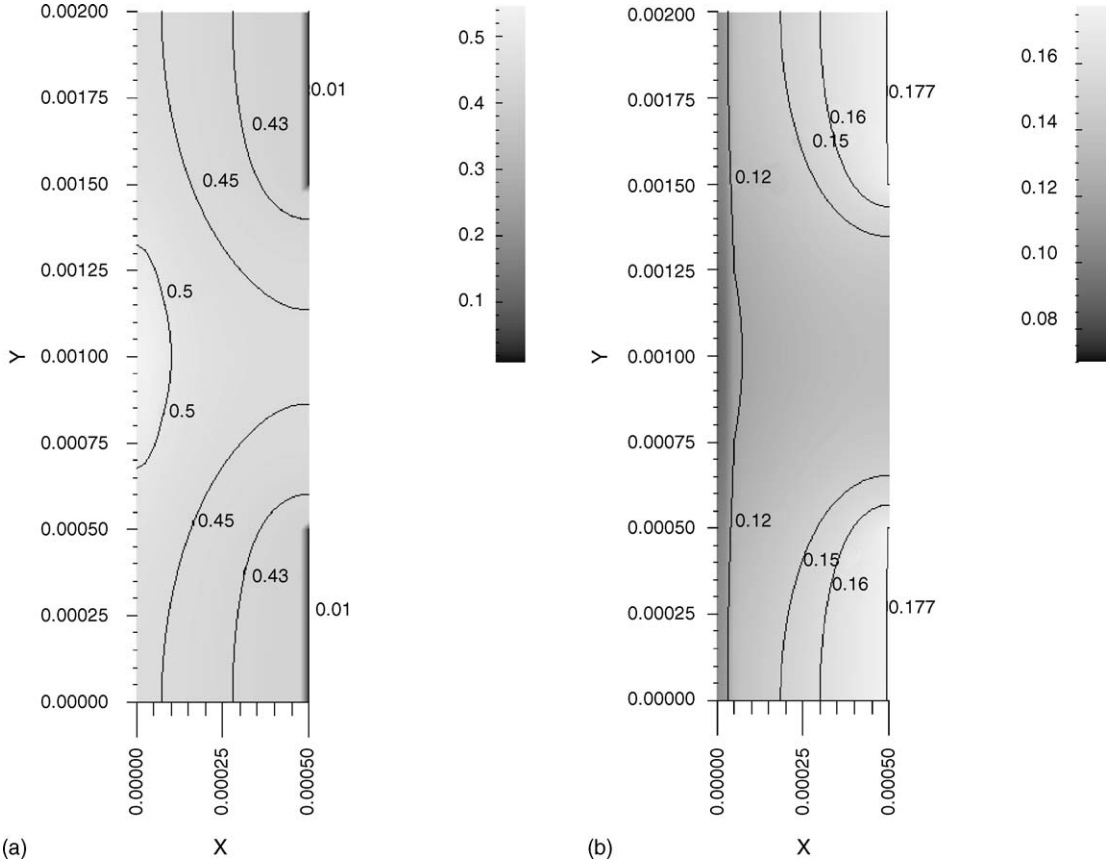

Fig. 18. Liquid water saturation and oxygen concentration profile in the electrode at 0.5 V cell voltage for the drainage curve—conventional gas distributor (X, electrode thickness and Y, electrode height): (a) S_w; (b) $x_g^{O_2}$.

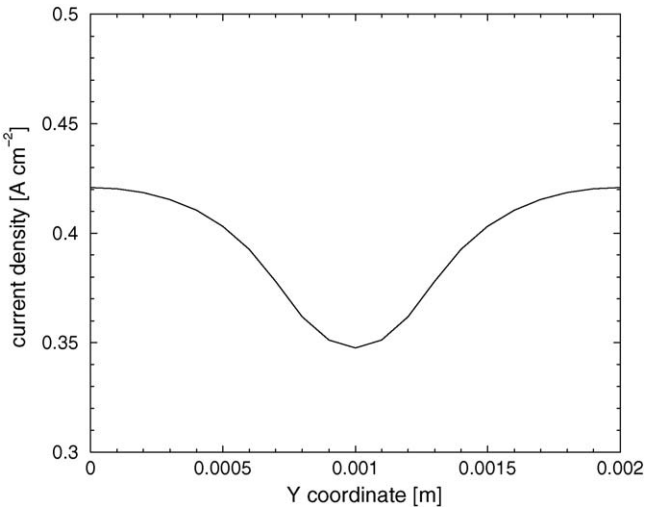

Fig. 19. Current density distribution at the catalyst layer–membrane interface at 0.5 V cell voltage for the drainage curve—conventional gas distributor.

5.3. Drainage curve results

In order to obtain the system response by allowing higher liquid saturations, the extension of the drainage curve presented in Fig. 8 is used for the calculations. For the fitting curve selected, the transition from the hydrophobic to the hydrophilic region occurs at a liquid water saturation of about 0.41. This value is interpreted as the lowest water saturation, under which a pressure in the gas phase has to be applied in order to replace the water phase trapped in the pore system.

Fig. 17 shows the resulting polarization curve obtained for the drainage data, compared again with the measured data for the conventional gas distributor. In this case the model prediction matches the experimental values very good, which means that in practice higher liquid water saturations are to be expected in the electrode. The model can hence correctly reproduce the hindering effect of the liquid phase on the cell performance.

The drainage curve can thus better represent the real cell operation than the imbibition one. This is also expected by the fact that, after a given operation time, liquid water will be present at the fuel cell cathode and the drainage process, that is taking place rather than purely imbibition, is more significant for the liquid water distribution.

Fig. 18 shows the steady-state oxygen concentration and liquid water saturation profiles considering the drainage curve given in Fig. 8 for a cell voltage of 0.5 V. As expected, high liquid water saturation values are obtained, with a correspondingly lower current density distribution as shown in Fig. 19, with an average value of 0.40 A cm^{-2} at 0.5 V cell voltage.

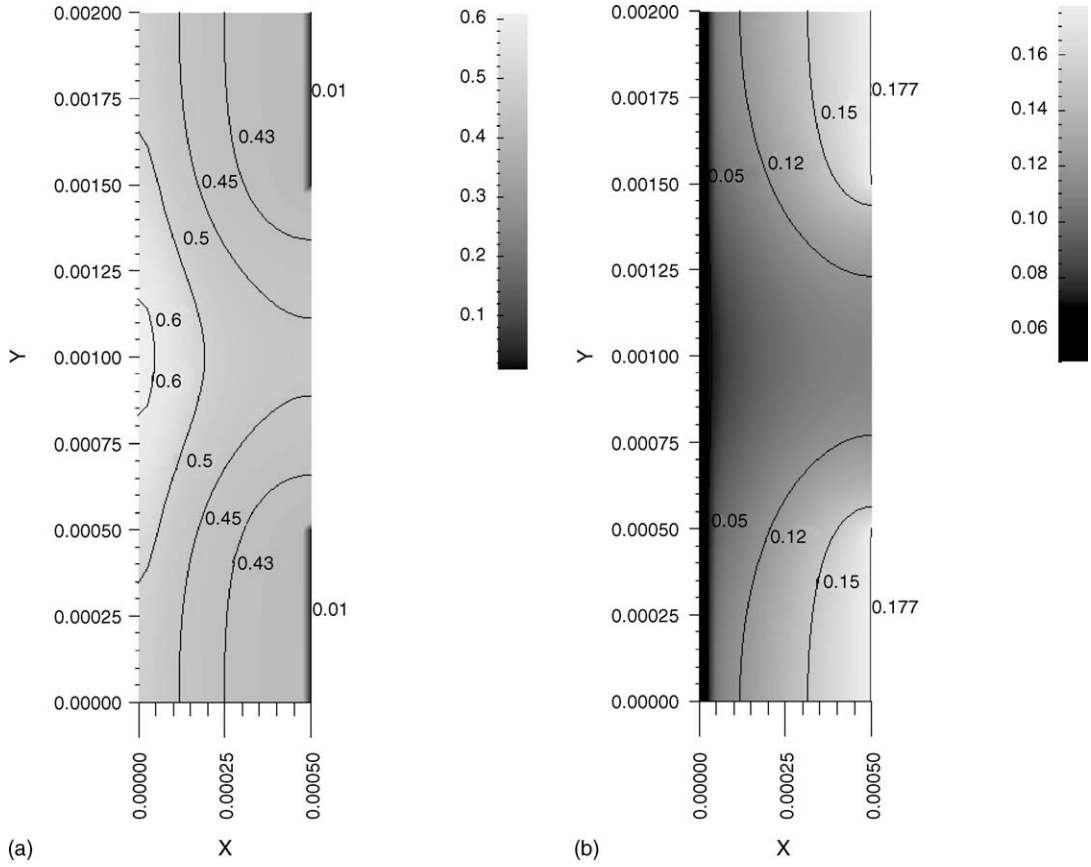

Fig. 20. Liquid water saturation and oxygen concentration profile in the electrode at 0.3 V cell voltage for the drainage curve—conventional gas distributor (X, electrode thickness and Y, electrode height): (a) S_w; (b) $x_g^{O_2}$.

Fig. 20 shows the steady-state oxygen concentration and liquid water saturation profiles considering the drainage curve for a cell voltage of 0.3 V. At this lower voltage, the liquid water saturation in the electrode increases upon 60%.

6. Summary and conclusions

A two-dimensional, two-phase, non-isothermal, multicomponent model was developed for the cathode of a PEM fuel cell, which can be applied using both conventional and interdigitated gas distributors. In a PEM fuel cell, where the membrane needs to be humidified with liquid water to provide sufficient protonic conductivity, the water management at the cathode, where water is being produced by the electrochemical reaction and an excess can hinder the oxygen diffusion, becomes a difficult task. The performance of the fuel cell is highly influenced by the presence of liquid water and its removal rate, particularly at high current densities. The water accumulation is strongly influenced by both the gas flow configuration and the wetting properties of the cathode gas diffusion material.

Due to the lack in physical properties for the commonly used electrodes, the most important properties affecting the hydrodynamics of liquid and gas flow in porous media have been determined experimentally. For the capillary behaviour an indirect method has been applied. In a first step the relative permeability data have been derived from mercury intrusion porosimetry measurements and corrected to water through the Laplace equation. It turned out however that a more detailed consideration of the partial wettability of the electrode backing is necessary to obtain agreement between simulation and experiments at high fuel cell loads. In future work the partially hydrophilic behaviour of the gas diffusion material should be closer investigated for an air–water system. For the relative permeability, new methods for the experimental determination are going to be part of the work on the next periods.

The increase in performance due to the faster water removal by the interdigitated flow distributor is correctly predicted by the model. However, due to the assumption of a purely hydrophobic character of the gas diffusion material, only low liquid water saturations are obtained. By considering a partially hydrophilic behaviour, as shown during the drainage process, high liquid saturations are present in the electrode yielding to mass transport limitations. Thus, the model predicts a decrease in performance due to the stronger hindering effect of the liquid phase on the oxygen transport which is in agreement with experimental results.

The suggested model predicts correctly the tendency of the different transport processes in the cathode, whereas the main difficulties in describing this system arise from the determination of the most important flow parameters, in particular wettability, capillarity and relative permeability, which will be closer investigated for these materials in future work. On the other side, also the correct description of the boundaries to the gas channel affecting the liquid water saturation is of great importance for the system description. The liquid water saturation value could be obtained from an equilibrium assumption under different operating conditions for the gas humidity. This should also be investigated in future work.

Acknowledgement

Financial support from the Deutsche Forschungsgemeinschaft (DFG) is gratefully acknowledged.

References

[1] K. Kordesch, G. Simader, Fuel Cells and their Applications, VCH, 1996.
[2] T.E. Springer, M.S. Wilson, S. Gottesfeld, Modelling and experimental diagnostics in polymer electrolyte fuel cells, J. Electrochem. Soc. 140 (12) (1993) 3513–3526.
[3] T.V. Nguyen, A gas distributor design for proton-exchange-membrane fuel cells, J. Electrochem. Soc. 143 (5) (1996) L103–L105.
[4] D.M. Bernardi, M.W. Verbrugge, A Mathematical model of the solid-polymer–electrolyte fuel cell, J. Electrochem. Soc. 139 (9) (1992) 2477–2490.
[5] J.S. Yi, T.V. Nguyen, An along-the-channel model for proton exchange membrane fuel cells, J. Electrochem. Soc. 145 (4) (1998) 1149–1159.
[6] J.S. Yi, T.V. Nguyen, Multicomponent transport in porous electrodes of proton exchange membrane fuel cells using the interdigitated gas distributors, J. Electrochem. Soc. 146 (1) (1999) 38–45.
[7] A. Kazim, H. Liu, P. Forges, Modelling of performance of PEM fuel cells with conventional and interdigitated flow fields, J. Appl. Electrochem. 29 (1999) 1409–1416.
[8] S. Dutta, S. Shimpalee, J.W.V. Zee, Three-dimensional numerical simulation of straight channel PEM fuel cells, J. Appl. Electrochem. 30 (2000) 135–146.
[9] K.V. Zhukovsky, Three-dimensional model of oxygen transport in a porous diffuser of a PEM fuel cell, AIChE J. 49 (12) (2003) 3029–3036.
[10] G. Hu, J. Fan, S. Chen, Y. Liu, K. Cen, Three-dimensional numerical analysis of proton exchange membrane fuel cells (PEMFCs) with conventional and interdigitated flow fields, J. Power Source 136 (2004) 1–9.
[11] V. Gurau, H. Liu, S. Kakac, Two-dimensional model for proton exchange membrane fuel cells, AIChE J. 44 (11) (1998) 2410–2422.
[12] S. Shimpalee, S. Dutta, Numerical prediction of temperature distribution in PEM fuel cells, Numeric Heat Transfer Part A 38 (2000) 111–128.
[13] W. He, J. Yi, T.V. Nguyen, Two-phase flow model of the cathode of PEM fuel cells using interdigitated flow fields, AIChE J. 46 (10) (2000) 2053–2064.
[14] Z.H. Wang, C.Y. Wang, K.S. Chen, Two-phase flow and transport in the air cathode of proton exchange membrane fuel cells, J. Power Source 94 (2001) 40–50.
[15] D. Natarajan, T.V. Nguyen, A two-dimensional, two-phase, multicomponent, transient model for the cathode of a proton exchange membrane fuel cell using conventional gas distributors, J. Electrochem. Soc. 148 (12) (2001) A1324–A1335.
[16] D. Natarajan, T.V. Nguyen, Three-dimensional effects of liquid water flooding in the cathode of a PEM fuel cell, J. Power Source 115 (2003) 66–80.
[17] T. Berning, D.M. Lu, N. Djilali, Three-dimensional computational analysis of transport phenomena in a PEM fuel cell, J. Power Source 106 (2002) 284–294.
[18] T. Berning, N. Djilali, A 3D, multiphase, multicomponent model of the cathode and anode of a PEM fuel cell, J. Electrochem. Soc. 150 (12) (2003) A1589–A1598.
[19] G. Lin, W. He, T.V. Nguyen, Modeling liquid water effects in the gas diffusion and catalyst layers of the cathode of a PEM fuel cell, J. Electrochem. Soc. 151 (12) (2004) A1999–A2006.
[20] J.H. Nam, M. Kaviany, Effective diffusivity and water-saturation distribution in single- and two-layer PEMFC diffusion medium, Int. J. Heat Mass Transfer 46 (2003) 4595–4611.
[21] U. Pasaogullari, C. Wang, Liquid water transport in gas diffusion layer of polymer electrolyte fuel cells, J. Electrochem. Soc. 151 (3) (2004) A399–A406.

[22] J. Ihonen, M. Mikkola, G. Lindbergh, Flooding of gas diffusion backing in PEFCs: physical and electrochemical characterization, J. Electrochem. Soc. 151 (8) (2004) A1152–A1161.
[23] J. Bear, Dynamic of Fluids in Porous Media, Dover Publications, Inc., 1988.
[24] T.E. Springer, T.A. Zawodzinski, M.S. Wilson, S. Gottesfeld, Characterization of polymer electrolyte fuel cells using ac impedance spectroscopy, J. Electrochem. Soc. 143 (2) (1996) 587–599.
[25] M. Wöhr, Instationäres, thermodynamisches Verhalten der Polymermembran-Brennstoffzelle, PhD Thesis, University of Stuttgart, 1998.
[26] R. Helmig, Multiphase Flow and Transport Processes in the Subsurface—A Contribution to the Modeling of Hydrosystems, Springer Verlag, 1997.
[27] M.C. Leverett, Capillary behaviour in porous solids, AIME 142 (1941) 152–169.
[28] M.T.V. Genuchten, A closed-form equation for predicting the hydraulic conductivity of unsaturated soils, Soil Sci. Soc. Am. J. 44 (1980) 892–898.
[29] R.H. Brooks, A.T. Corey, Hydraulic Properties of Porous Media, Hydrol. Pap. 3, Colorado State University, 1964.
[30] C. Wieser, Stromdichteverteilung und Leistungsverhalten der Polymerelektrolyt-Brennstoffzelle, PhD Thesis, University of Stuttgart, 2001.
[31] R. Helmig, H. Class, H. Huber, H. Sheta, R. Ewing, R. Hinkelmann, H. Jakobs, P. Bastian, Architecture of the modular program system MUFTE_UG for simulating multiphase flow and transport processes in heterogeneous porous media, Math. Geol. 2 (1998).
[32] P. Bastian, K. Birken, S. Lang, K. Johannsen, N. Neuss, H. Rentz-Reichert, C. Wieners, UG: a flexible software toolbox for solving partial differential equations, in: Computing and Visualization in Science, vol. 1, Springer Verlag, 1997, pp. 27–40.
[33] P. Bastian, R. Helmig, Efficient fully-coupled solution techniques for two phase flow in porous media. parallel multigrid solution and large scale computations, Adv. Water Resour. 23 (1999) 199–216.
[34] H. Class, R. Helmig, P. Bastian, Numerical simulation of non-isothermal multiphase multicomponent processes in porous media. 1. An efficient solution technique, Adv. Water Resour. 25 (2002) 533–550.
[35] P. Bastian, Numerical computation of multiphase flows in porous media, Habilitation Thesis, Technische Fakultät, Christian–Albrechts–Universität Kiel, 1999.
[36] H. Lechner, Die Kontaktwinkelmessung: Ein Verfahren zur Bestimmung der freien Grenzflächenenergie von Festkörpern, Krüss GmbH Süd, Wissenschaftliche Laborgeräte, Stephanskirchen, Germany, 1988.
[37] J. Drelich, J.D. Miller, R.J. Good, The effect of drop (bubble) size on advancing and receding contact angles for heterogeneous and rough solid surfaces as observed with sessile-drop and captive-bubble techniques, J. Colloid Interface Sci. 179 (1996) 37–50.
[38] W.R. Purcell, Capillary pressures—their measurement using Mercury and the calculation of permeability therefrom, Petrol. Trans. AIME T. P. 2544 (1949) 39–46.
[39] E. Wicke, R. Kallenbach, Die Oberflächendiffusion von Kohlendioxid in aktiven Kohlen, Kolloid-Zeitung 97 (2) (1941) 135–151.
[40] H. Schubert, Kapillarität in porösen Feststoffsystemen, Springer Verlag, 1982.
[41] H. Sheta, Simulation von Mehrphasenvorgängen in porösen Medien unter Einbeziehung von Hysterese-Effekten, PhD Thesis, University of Stuttgart, 1999.
[42] N.T. Burdine, Relative permeability calculations from pore-size distribution data, Tech. Rep., Petrol. Trans. AIME (1953).
[43] A. Parthasarathy, S. Srinivasan, J. Appleby, C. Martin, Pressure dependence of the oxygen reduction reaction at the platinum microelectrode–Nafion interface: electrode kinetics and mass transport, J. Electrochem. Soc. 139 (10) (1992) 2856–2862.
[44] F. Meier, Stofftransport in Polymerelektrolyt-Membranen für Brennstoffzellen—Experimentelle Untersuchung, Modellierung und Simulation, PhD Thesis, University of Stuttgart, 2004.
[45] W. Neubrand, Modellbildung und Simulation von Elektromembranverfahren, PhD Thesis, University of Stuttgart, 1999.
[46] W. He, G. Lin, T.V. Nguyen, Diagnostic tool to detect electrode flooding in proton-exchange-membrane fuel cells, AIChE J. 49 (12) (2003) 3221–3228.
[47] B. Thoben, A. Siebke, Influence of different gas diffusion layers on the water management of the PEFC cathode, J. New Mater. Electrochem. Syst. 7 (2004) 13–20.
[48] M. Acosta, Untersuchung von Elektrode–Membran–Elektrode (EME)-Einheiten und Gasverteilerstrukturen für PEM-Brennstoffzellen, Master's Thesis, Universität Stuttgart. Institut für Chemische Verfahrenstechnik, 2000.
[49] R. Reissner, B. Thoben, T. Kaz, M. Schulze, E. Gülzow, Degradation of the hydrophobicity of fuel cell electrodes, Proceedings of the Eighth UECT, Ulm, Germany, June 20–21, 2002.